Quasiparticle random-phase approximation calculations for $M1$ transitions with the noniterative finite-amplitude method and application to neutron radiative capture cross sections

Hirokazu Sasaki,* Toshihiko Kawano, and Ionel Stetcu
Theoretical Division, Los Alamos National Laboratory, Los Alamos, New Mexico 87545, USA

(Received 30 November 2022; revised 14 March 2023; accepted 12 May 2023; published 24 May 2023)

We derive the equations of quasiparticle random-phase approximation (QRPA) based on the finite amplitude method with the Hartree-Fock+Bardeen–Cooper–Schrieffer (HF+BCS) single-particle states, and calculate the magnetic dipole ($M1$) transition for deformed gadolinium isotopes. Our QRPA calculation shows both large spin-flip transitions in the 5 to 10 MeV excitation energy and the low energy orbital transition that would correspond to the $M1$ scissors mode observed in nuclear experiments. Then, we calculate neutron capture reactions based on the statistical Hauser-Feshbach theory with the photoabsorption cross sections of even-even nuclei given by QRPA. We find that the capture cross section is enhanced due to the contribution from the low energy $M1$ transition although the calculated capture cross section still underestimates the experimental data. This issue in the calculated capture cross section could be improved by uncertainties of the low energy $E1$ transition neglected in our QRPA calculation.

DOI: 10.1103/PhysRevC.107.054312

I. INTRODUCTION

Neutron-capture reactions are essential for the nucleosynthesis of heavy elements, and their cross section data are needed to calculate nuclear abundances in astrophysical sites [1]. It is theoretically predicted that many unstable nuclei are produced through the rapid neutron capture process (r process) [2] before β decays in core-collapse supernovae and neutron star mergers, which contributes to the galactic chemical evolution of about half of heavy elements [3]. The (n, γ) reaction is also important for neutrino-induced nucleosynthesis inside core-collapse supernovae such as the νp process [4–6] and the ν process [7–9]. The experimental data for the capture reactions are mainly limited to stable nuclei, so a reliable theoretical calculation is required to study the origin of elements.

In the neutron capture reaction, a compound nucleus is formed after the interaction of an incoming neutron with the target nucleus and finally decays by emitting several γ rays. The statistical Hauser-Feshbach theory [10] can estimate the decay rates of such a compound nucleus, and calculate neutron capture cross sections with transmission coefficients for all possible competing channels. The transmission coefficient of the outgoing γ ray is calculated with γ-ray strength functions [11] of electric and magnetic giant resonances under the Brink-Axel hypothesis [12]. Instead of a standard Lorentzian using the giant dipole resonance (GDR) parameters, a generalized Lorentzian [11,13] is proposed empirically and widely used to calculate the γ-ray strength function of the electric dipole ($E1$) transition. The magnetic dipole ($M1$) transition also has non-negligible impact on the capture cross section. In particular, the $M1$ scissors mode, which is often observed in a few MeV energy region for strongly deformed nuclei, can enhance the capture cross section [14–16].

The $M1$ scissors mode is induced by the collective motion of protons and neutrons inside a deformed nucleus associated with the orbital angular momentum operator, and it was first observed in an electron scattering experiment [17]. Since then, the $M1$ scissors mode has been found in various rare-earth nuclei and actinides [18].

Calculating capture reactions without any phenomenological parameters as used in the conventional γ-ray strength function is possible when we employ the strength of the $M1$ transition obtained in the density functional theory (DFT) [19]. DFT interprets the giant resonance as coherent superpositions of $1p$-$1h$ excitations in a nuclear many-body system, and the transition strength of such a collective excitation is microscopically calculated with random-phase approximation (RPA) [19]. In order to introduce pairing correlations, essential for description of open-shell nuclei, RPA must be extended to quasiparticle RPA (QRPA) [20]. Various collective excitations have been calculated in (Q)RPA [21]. Fully self-consistent (Q)RPA approaches with the Skyrme forces have been applied to the $E1$ transition [22–25] as well as the $M1$ transition [26–31]. Although the (Q)RPA for the $E1$ transition well reproduces the resonance energy of GDR in heavy nuclei, it is often reported that the calculated spin-flip $M1$ giant resonance unsatisfactory agrees with experimental data and depends on parametrizations of Skyrme force [27]. The spin densities in the Skyrme force increase the resonance peak of the spin-flip transition [26].

The finite amplitude method (FAM) [32,33] is an efficient way to solve the fully self-consistent (Q)RPA equation

*hsasaki@lanl.gov

when applied to various multipole collective excitations [23–25,34–36]. The FAM approach was extended to the relativistic framework [37,38], the proton-neutron FAM (*pn*FAM) for weak interactions [39–42], and the fission calculation [43]. The framework of FAM-RPA is used to derive the RPA matrices for Skyrme functionals by the explicit linearization of residual interactions [25]. The technique of such noniterative FAM-RPA can be used to derive QRPA matrices based on the framework of FAM-QRPA that enables the calculation of the $M1$ transition for open-shell and deformed nuclei without any iterative procedure to obtain forward and backward amplitudes in other conventional FAM-QRPA.

In this paper, we derive the QRPA matrices based on noniterative FAM-QRPA and calculate the $M1$ transition for deformed gadolinium isotopes. This work is an extension of our noniterative FAM-RPA [25] to the QRPA framework, while it neglects the pairing fluctuation. The microscopically calculated photoabsorption cross sections for the $E1$ and $M1$ transitions with our QRPA approach are then fed into the Hauser-Feshbach calculations as the γ-ray transmission coefficients to obtain the neutron capture cross sections. Then, we compare the calculated result with available experimental data.

II. THEORY

A. Finite amplitude method (FAM)

We briefly review the general framework of the finite amplitude method in QRPA. In FAM-QRPA, the forward and backward amplitudes of a frequency ω are calculated through [24,33]

$$(E_\mu + E_\nu - \omega)X_{\mu\nu}(\omega) + \delta H^{20}_{\mu\nu}(\omega) = -F^{20}_{\mu\nu}(\omega), \quad (1)$$

$$(E_\mu + E_\nu + \omega)Y_{\mu\nu}(\omega) + \delta H^{02}_{\mu\nu}(\omega) = -F^{02}_{\mu\nu}(\omega), \quad (2)$$

where $X(Y)$ is the forward (backward) amplitude, E_μ is an energy eigenvalue of a Bogoliubov quasiparticle state μ, $\delta H^{20(02)}_{\mu\nu}(\omega)$ is the two-quasiparticle component of residual interactions, and $F^{20(02)}_{\mu\nu}(\omega)$ is the two-quasiparticle component of the external field. For a simple notation, hereafter, we drop the index ω in matrices except when necessary. The residual interaction is calculated with the forward and backward amplitudes, and these amplitudes are determined by solving Eqs. (1) and (2) iteratively at each ω. The obtained amplitudes are used to calculate the transition strength [33]

$$\frac{\mathrm{d}B(\omega;F)}{\mathrm{d}\omega} = -\frac{1}{2\pi}\mathrm{Im}\sum_{\mu\nu}\left(F^{20*}_{\mu\nu}X_{\mu\nu} + F^{02*}_{\mu\nu}Y_{\mu\nu}\right), \quad (3)$$

where the imaginary part of ω corresponds to the Lorentzian width characterizing the width of the transition strength. Hereafter, we assume that the external field F does not change the isospin of nucleons.

B. QRPA equations

Instead of solving Eqs. (1) and (2) by an iterative procedure, we derive the QRPA equation with the well-known QRPA matrices A and B from the explicit linearization of the residual interaction in Eqs. (1) and (2) as in FAM-RPA [25]. We use the quasiparticle states of Hamiltonian in the Hartree-Fock+Bardeen–Cooper–Schrieffer (HF+BCS) calculation instead of the Hartree-Fock-Bogoliubov (HFB) calculation. In HF+BCS, the HFB matrices, such as U and V, only allow the mixing between a single-particle state k, and the corresponding time-reversed state $\bar{k}$. These matrices can be described in the coordinate space $\vec{r}$, the spin space σ, and the isospin $q(= n, p)$ [19,20]:

$$U_\mu(\vec{r},\sigma,q) = u_\mu\phi_\mu(\vec{r},\sigma,q), \quad (4)$$

$$V_\mu(\vec{r},\sigma,q) = -v_\mu\phi^*_{\bar{\mu}}(\vec{r},\sigma,q), \quad (5)$$

where $u_\mu \geqslant 0$ and $v_\mu \geqslant 0$ are the BCS parameters, and $\phi_\mu(\vec{r},\sigma,q) \equiv \phi^q_\mu$ is the single-particle state of the HF Hamiltonian h_0 satisfying $h_0\phi^q_\mu = \epsilon_\mu\phi^q_\mu$. To derive Eq. (5), we use properties of the time-reversal symmetry of the HF single-particle states, $\phi^q_{\bar{\mu}} = T\phi^q_\mu$, and $\phi^q_{\bar{\mu}} = T^2\phi^q_\mu = -\phi^q_\mu$, where T is the time-reversal operator [44]. In the case of a Hermitian one-body external field F [19,33], the quasiparticle components in Eqs. (1) and (2) are given by

$$\begin{aligned} F^{20}_{\mu\nu} &= (U^\dagger f V^* - V^\dagger f^T U^*)_{\mu\nu} \\ &= -u_\mu v_\nu f^q_{\mu\bar{\nu}} + u_\nu v_\mu f^q_{\nu\bar{\mu}} \\ &= -\zeta^\tau_{\mu\nu} f^q_{\mu\bar{\nu}}, \end{aligned} \quad (6)$$

$$\begin{aligned} F^{02}_{\mu\nu} &= (U^T f^T V - V^T f U)_{\mu\nu} \\ &= -u_\mu v_\nu f^q_{\bar{\nu}\mu} + u_\nu v_\mu f^q_{\bar{\mu}\nu} \\ &= -\zeta^\tau_{\mu\nu} f^q_{\bar{\nu}\mu}, \end{aligned} \quad (7)$$

where $\zeta^\tau_{\mu\nu} = u_\mu v_\nu + \tau u_\nu v_\mu$ with $\tau = \pm 1$ and $f^q_{\mu\nu} = \int \mathrm{d}^3 r \phi^{q*}_\mu F \phi^q_\nu$. From the second lines to the third lines in the above equations, we assume the time-reversal invariance for the external field, $TFT^{-1} = \tau F$, and use a relation, $f^q_{\nu\bar{\mu}} = -\tau f^q_{\mu\bar{\nu}}$ [20,45].

We ignore the contributions from the residual interactions of the BCS pairing gap $\delta\Delta^\pm$ and the abnormal density $\delta\kappa^\pm$ [33]. Then, as in Eqs. (6) and (7), quasiparticle components of the residual interaction in Eqs. (1) and (2) are given by

$$\delta H^{20}_{\mu\nu} = -\zeta^+_{\mu\nu}\delta h^{\mathrm{even}}_{\mu\bar{\nu}} - \zeta^-_{\mu\nu}\delta h^{\mathrm{odd}}_{\mu\bar{\nu}}, \quad (8)$$

$$\delta H^{02}_{\mu\nu} = -\zeta^+_{\mu\nu}\delta h^{\mathrm{even}}_{\bar{\nu}\mu} - \zeta^-_{\mu\nu}\delta h^{\mathrm{odd}}_{\bar{\nu}\mu}, \quad (9)$$

where $\delta h^{\mathrm{even(odd)}}$ is the residual interaction composed of time-even (odd) fields composed of the HF+BCS single-particle states. In FAM-QRPA, these residual interactions are calculated with a small parameter η following the same procedure to obtain $\delta h(\omega)$ and $\delta\rho(\omega)$ in Ref. [33]. In the limit of $\eta \to 0$, such calculated residual interactions can be expressed as the linear combination of X and Y as done in

FAM-RPA [25]. Then, the QRPA equation is derived from Eqs. (1) and (2):

$$\begin{pmatrix} A-\omega & B \\ B^* & A^*+\omega \end{pmatrix}\begin{pmatrix} X^{q'}_{\alpha\beta} \\ Y^{q'}_{\alpha\beta} \end{pmatrix} = -\zeta^{\tau}_{\mu\nu}\begin{pmatrix} f^{q}_{\mu\nu} \\ f^{q}_{\nu\mu} \end{pmatrix}, \tag{10}$$

$$A^{q,q'}_{\mu\nu,\alpha\beta} = (E_\mu+E_\nu)\delta_{\mu\alpha}\delta_{\nu\beta}+\zeta^{+}_{\mu\nu}\zeta^{+}_{\alpha\beta}\int \mathrm{d}^3r\,\phi^{q*}_{\mu}\frac{\partial h^{\mathrm{even}}_{q}}{\partial\left(\eta\zeta^{+}_{\alpha\beta}X^{q'}_{\alpha\beta}\right)}\bigg|_{\eta=0}\phi^{q}_{\nu}+\zeta^{-}_{\mu\nu}\zeta^{-}_{\alpha\beta}\int \mathrm{d}^3r\,\phi^{q*}_{\mu}\frac{\partial h^{\mathrm{odd}}_{q}}{\partial\left(\eta\zeta^{-}_{\alpha\beta}X^{q'}_{\alpha\beta}\right)}\bigg|_{\eta=0}\phi^{q}_{\nu}, \tag{11}$$

$$B^{q,q'}_{\mu\nu,\alpha\beta} = \zeta^{+}_{\mu\nu}\zeta^{+}_{\alpha\beta}\int \mathrm{d}^3r\,\phi^{q*}_{\mu}\frac{\partial h^{\mathrm{even}}_{q}}{\partial\left(\eta\zeta^{+}_{\alpha\beta}Y^{q'}_{\alpha\beta}\right)}\bigg|_{\eta=0}\phi^{q}_{\nu}+\zeta^{-}_{\mu\nu}\zeta^{-}_{\alpha\beta}\int \mathrm{d}^3r\,\phi^{q*}_{\mu}\frac{\partial h^{\mathrm{odd}}_{q}}{\partial\left(\eta\zeta^{-}_{\alpha\beta}Y^{q'}_{\alpha\beta}\right)}\bigg|_{\eta=0}\phi^{q}_{\nu}, \tag{12}$$

$$E_\mu = \sqrt{(\epsilon_\mu-\lambda)^2+\Delta^2_\mu}, \tag{13}$$

where h_q is the time-dependent Hartree-Fock (TDHF) Hamiltonian of the nucleon q, and $h^{\mathrm{even(odd)}}_q$ is the time-even(odd) part of h_q, λ is the Fermi energy, and Δ_μ is the pairing gap of single-particle state μ, and the size of the configuration space is restricted to $\mu \geqslant \nu,\ \alpha \geqslant \beta$. When we derive Eqs. (10)–(13), we assume the time-reversal symmetry of the HF Hamiltonian, $Th_0T^{-1} = h_0$, and change the definition of the amplitudes in Eqs. (1) and (2) as

$$X_{\mu\nu} \to -X_{\mu\bar{\nu}},\ Y_{\mu\nu} \to -Y_{\mu\bar{\nu}}, \tag{14}$$

which facilitates to extend an existing RPA code to the full QRPA calculation. The QRPA equation of Eq. (10) reproduces the RPA equation in Ref. [25] when we impose $\epsilon_{\mu(\alpha)} > \lambda > \epsilon_{\nu(\beta)}$ and $u_{\mu(\alpha)} = v_{\nu(\beta)} = 1$, which results in $\zeta^{\pm}_{\mu\nu} = \zeta^{\pm}_{\alpha\beta} = 1$ in Eqs. (10)–(12) and $\Delta_\mu = 0$ in Eq. (13).

The integrands in Eqs. (11) and (12) are calculated with the Skyrme forces composed of the HF+BCS single-particle states. For example, the contribution from the effective mass m^*_q [46] to the integral term proportional to $\zeta^{+}_{\mu\nu}\zeta^{+}_{\alpha\beta}$ in Eq. (11) is given by

$$\begin{aligned}
&\int \mathrm{d}^3r\,\phi^{q*}_{\mu}\nabla\cdot\left(\frac{\partial}{\partial\left(\eta\zeta^{+}_{\alpha\beta}X^{q'}_{\alpha\beta}\right)}\frac{-\hbar^2}{2m^*_q}\right)_{\eta=0}\nabla\phi^{q}_{\nu} \\
&\quad= \int \mathrm{d}^3r\left\{\frac{\partial(b_1\rho_n+b_1\rho_p-b'_1\rho_q)}{\partial\left(\eta\zeta^{+}_{\alpha\beta}X^{q'}_{\alpha\beta}\right)}\right\}_{\eta=0}\nabla\phi^{q*}_{\mu}\cdot\nabla\phi^{q}_{\nu} \\
&\quad= (b_1-\delta_{qq'}b'_1)\int \mathrm{d}^3r\,\phi^{q'*}_{\beta}\phi^{q'}_{\alpha}\nabla\phi^{q*}_{\mu}\cdot\nabla\phi^{q}_{\nu},
\end{aligned} \tag{15}$$

$$\begin{aligned}
\rho_q &= \sum_{\alpha\in q} v^2_\alpha\left|\phi^{q}_{\alpha}\right|^2 \\
&\quad+\eta\sum_{\substack{\alpha\beta\,\in\, q \\ \alpha\,\geqslant\,\beta}}\zeta^{+}_{\alpha\beta}\left(\phi^{q*}_{\beta}\phi^{q}_{\alpha}X^{q}_{\alpha\beta}+\phi^{q*}_{\alpha}\phi^{q}_{\beta}Y^{q}_{\alpha\beta}\right)+O(\eta^2),
\end{aligned} \tag{16}$$

where b_1 and b'_1 are coefficients in the Skyrme force [46], and ρ_q is the density of nucleon q. The symmetrical properties such as $X^{q}_{\alpha\beta} = X^{q}_{\bar{\beta}\bar{\alpha}}$, $Y^{q}_{\alpha\beta} = Y^{q}_{\bar{\beta}\bar{\alpha}}$, and $\phi^{q*}_{\bar{\alpha}}\phi^{q}_{\bar{\beta}} = \phi^{q*}_{\beta}\phi^{q}_{\alpha}$ are used to derive the second line of Eq. (16). As implied in Eq. (15), integral terms in the QRPA matrices can be calculated by multiplying $\zeta^{\pm}_{\mu\nu}\zeta^{\pm}_{\alpha\beta}$ with the residual interaction derived in the same way as RPA calculation (e.g., Eqs. (32) and (39) in Ref. [25]). The ρ_q in Eq. (16) contains a factor $\zeta^{+}_{\alpha\beta}$ in the linear term of η and such a property is also confirmed in other time-even fields such as the spin-orbit density $\vec{J}_q$, and the kinetic energy density τ_q [46]. On the other hand, the time-odd fields such as the current density $\vec{j}_q$ and the spin density $\vec{s}_q$ [46] include a factor $\zeta^{-}_{\alpha\beta}$ in $O(\eta)$ [e.g., see Eq. (A2)]. $\zeta^{+}_{\alpha\beta}$ and $\zeta^{-}_{\alpha\beta}$ in Eqs. (11) and (12) originated from the linear terms of η in time-even and time-odd fields. Although our approach is applicable only if the time-reversal symmetry of the HF Hamiltonian is satisfied, we can calculate the QRPA matrices in Eqs. (11) and (12) without any uncertainty of small parameter η as used in the conventional matrix-FAM (m-FAM) [47]. In our explicit linearization with $\eta \to 0$, we can apparently show that the matrix A (B) is Hermitian (symmetric) [25], which are general properties of (Q)RPA matrices [19] and useful to test numerical calculations.

The frequency ω in Eq. (10) is decomposed into real and imaginary parts: $\omega = E + i\gamma/2$, where E is the incoming photon energy and γ is the Lorentzian width. The signs of τ in Eqs. (6) and (7) are negative (positive) for the $M1$ ($E1$) operator due to the time-odd (even) operator.

The forward and backward amplitudes are used to calculate the transition strength. In our QRPA, the transition strength of Eq. (3) is described by

$$\frac{\mathrm{d}B(\omega;F)}{\mathrm{d}\omega} = -\frac{1}{\pi}\mathrm{Im}\sum_{\substack{\mu\nu\in q \\ \mu\geqslant\nu}}\zeta^{\tau}_{\mu\nu}\left(f^{q*}_{\mu\nu}X^{q}_{\mu\nu}+f^{q*}_{\nu\mu}Y^{q}_{\mu\nu}\right), \tag{17}$$

where we use Eqs. (6), (7), and (14). Then, the photoabsorption cross section of the $M1$ transition is given by [25]

$$\sigma_{\mathrm{abs}}(E;M1) = \frac{16\pi^3}{9\hbar c}E\sum_{K=0,\pm1}\frac{\mathrm{d}B(\omega;M_K)}{\mathrm{d}\omega}, \tag{18}$$

where M_K is the $M1$ operator written as

$$M_K = \mu_N\sum_{i=1}^{A}\left(g^{(i)}_{s}\frac{\vec{\sigma}_i}{2}+g^{(i)}_{l}\vec{l}_i\right)\cdot\nabla(r_iY_{1K}(\theta_i,\varphi_i)), \tag{19}$$

where the (r_i,θ_i,φ_i) is the spherical coordinate of nucleon i, and $g^{(i)}_{l} = 0(1)$ and $g^{(i)}_{s} = -3.826(5.586)$ for

neutrons (protons). The photoabsorption cross section of the $E1$ transition is calculated in the same way as Eq. (18) with the $E1$ operator $D_K(K = 0, \pm 1)$ [25] instead of M_K.

C. Elimination of spurious modes

The (Q)RPA theory has spurious modes at zero energy ($\omega = 0$) corresponding to the collective motion of the whole nucleus associated with the violation of symmetries such as translational and rotational symmetries in the intrinsic Hamiltonian [19]. In (Q)RPA calculations, such a spurious mode usually appears at low energy and couples with the physical states due to the discretized coordinate space and the limited size of the configuration space [28,32,48]. The admixture of the spurious mode can be eliminated with the Hermitian broken-symmetry operator P and the conjugate operator Q satisfying $[Q, P] = i\hbar$. In order to remove the spurious mode, we renormalize the Hermitian external field F with a description similar to Ref. [28]:

$$\tilde{F} = F - \frac{i}{\hbar} \langle 0| [P, F] |0\rangle Q + \frac{i}{\hbar} \langle 0| [Q, F] |0\rangle P, \tag{20}$$

$$Q^{20}_{\mu\nu} = -(Q_0)^q_{\mu\bar{\nu}}, \quad P^{20}_{\mu\nu} = -(P_0)^q_{\mu\bar{\nu}}, \tag{21}$$

$$\begin{pmatrix} A & B \\ B^* & A^* \end{pmatrix} \begin{pmatrix} Q_0 \\ -Q_0^* \end{pmatrix} = -\frac{i\hbar}{M_0} \begin{pmatrix} P_0 \\ P_0^* \end{pmatrix}, \tag{22}$$

$$M_0 = 2\{\mathrm{Re}(P_0)(A + B)^{-1}\mathrm{Re}(P_0) + \mathrm{Im}(P_0)(A - B)^{-1}\mathrm{Im}(P_0)\}, \tag{23}$$

where M_0 is the inertia for the spurious mode, and $|0\rangle$ is the QRPA vacuum approximated by the HF+BCS ground state within the quasiboson approximation. For the $M1$ transition, the spurious mode appears at low energy due to the violation of the rotational symmetry for axially deformed nuclei and the spurious mode can be eliminated with the total angular momentum operator, $P = \sum_{i=1}^{A} (J_j)_i (j = x, y)$ in Eqs. (20)–(23). For the $E1$ transition, the translation of the center-of-mass induces the spurious modes, and Eqs. (20)–(23) are used to eliminate them with the total momentum operator, $P = \sum_{i=1}^{A} (-i\hbar)(\nabla_j)_i (j = x, y, z)$. We remark that such an elimination for the $E1$ transition is equivalent to imposing an effective charge of a neutron, $e^{(n)}_{\mathrm{eff}} = -eZ/A$, and that of a proton, $e^{(p)}_{\mathrm{eff}} = eN/A$ on the $E1$ operator [28]. We calculate the $E1$ transition with these effective charges on the $E1$ operator as in Ref. [25].

D. Microscopic calculations for neutron capture

We briefly review the calculation of neutron capture reactions following Ref. [15]. The photoabsorption cross sections for $E1$ and $M1$ transitions are used to calculate the neutron capture cross section based on the statistical Hauser-Feshbach model with the width fluctuation correction. In this statistical model, the formula for the radiative capture process, where a neutron and lumped γ-ray channels are involved, is written as

$$\sigma_{n\gamma}(E_n) = \frac{\pi}{k_n^2} \sum_{J\Pi} g_c \frac{T_n^{J\Pi} T_\gamma^{J\Pi}}{T_n^{J\Pi} + T_\gamma^{J\Pi}} W_{n\gamma}^{J\Pi}, \tag{24}$$

where E_n is the incident neutron energy, k_n is the incident neutron wave number, g_c is the spin statistical factor, $W_{n\gamma}$ is the width fluctuation correction factor [49], T_γ is the lumped γ-ray transmission coefficient, and T_n is the neutron transmission coefficient. The indices J and Π in the sum are the possible spin and the parity of the compound state.

The lumped γ-ray transmission coefficient is given by

$$T_\gamma^{J\Pi} = \sum_{j^\pi XL} \int_0^{E_0} \mathrm{d}E_x 2\pi E_\gamma^{2L+1} f_{XL}(E_\gamma) \rho(E_x, j^\pi), \tag{25}$$

where $E_0 = E_n + S_n$ is the total excitation energy, S_n is the neutron separation energy of the target nucleus, E_γ is the emitted photon energy, j^π is the spin and parity of the final state after the γ decay, $E_x = E_0 - E_\gamma$ is the excitation energy of the final state, ρ is the level density at E_x, and f_{XL} is the γ-ray strength function of the type of the transition $X(= E, M)$ and multipolarity L. Assuming the Brink-Axel hypothesis, the γ-ray strength function can be expressed in terms of the photoabsorption cross sections,

$$f_{XL}(E_\gamma) = \frac{\sigma_{\mathrm{abs}}(E_\gamma; XL)}{(2L + 1)(\pi\hbar c)^2 E_\gamma^{2L-1}}, \tag{26}$$

where $\sigma_{\mathrm{abs}}(E_\gamma; XL)$ is the photoabsorption cross section for XL transition. The above relation enables the application of the photoabsorption cross sections of QRPA to the microscopic calculation for the capture cross section without any experimental data of giant resonances.

III. RESULTS AND DISCUSSIONS

A. $M1$ transition

We solve the QRPA equation with the $M1$ operator, $M_K(K = 0, \pm 1)$ as the external field and calculate the transition strength and the photoabsorption cross section of $M1$ transition for ^{156}Gd following the description in Sec. II B. The single-particle states of HF+BCS are calculated as in the same setup in Ref. [50] where the axially symmetric harmonic oscillator basis [44] and the surface pairing interaction [51] are used for calculating the single-particle wave function. To calculate $\sum_{K=\pm1} \mathrm{d}B(\omega, M_K)/\mathrm{d}\omega$, we use a Hermitian operator $F = M_{+1} - M_{-1}$ with $P = -\sqrt{2}\sum_{i=1}^{A} (J_x)_i$ for the elimination of the spurious mode. The QRPA matrices are calculated as in Ref. [25] employing the Skyrme parameters of SLy4 [52]. Here, we consider the contribution from spin terms in the Skyrme force neglected in Ref. [25] that affects the spin-flip parts of the $M1$ transition [26]. Such spin terms are involved in the residual interaction from the time-odd Hamiltonian, h_q^{odd} in Eqs. (11) and (12), and the detailed description is shown in the Appendix.

The QRPA equation in Eq. (10) is solved from $E = 62.5$ keV to 20 MeV at every 62.5 keV with a fixed Lorentzian width $\gamma = 125$ keV. With the symmetry of indices in the forward and backward amplitudes, we impose an asymmetry

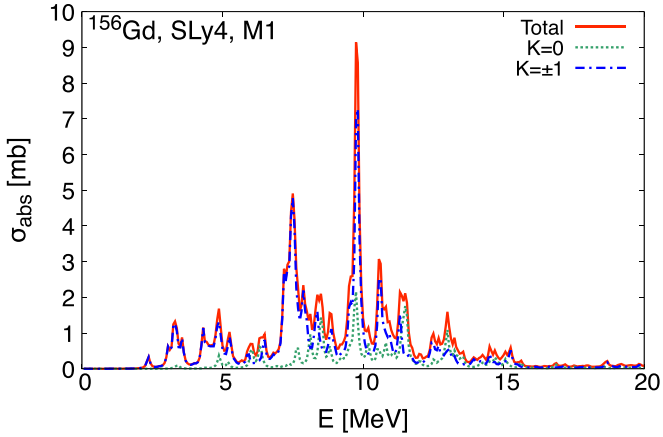

FIG. 1. The calculated photoabsorption cross sections of the $M1$ transitions for ^{156}Gd. The solid line shows the total photoabsorption cross section in Eq. (18). The dotted line is the component of $\mathrm{d}B(\omega, M_0)/\mathrm{d}\omega$, and the dot-dashed line is for $\sum_{K=\pm1} \mathrm{d}B(\omega, M_K)/\mathrm{d}\omega$.

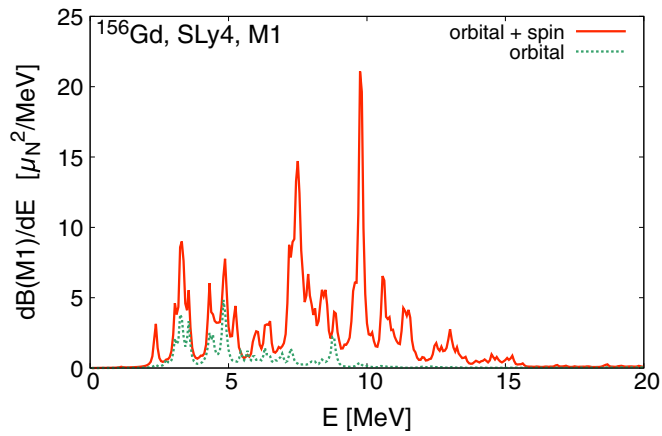

FIG. 2. The strength functions of the $M1$ transitions for ^{156}Gd with (solid line) and without (dotted line) the spin g factor g_s in Eq. (19).

in the pairs of quasiparticles, $\mu \geqslant \nu$ and restrict the size of the configuration space as $u_\mu^2, v_\nu^2 > 10^{-2}$, and $E_\mu + E_\nu < E_{\mathrm{cut}} = 50$ MeV. The $M1$ spurious mode appears at lower incoming photon energy even though E_{cut} is relatively high. However, the transition strength of the spurious mode is negligible due to the elimination of Eq. (20).

Figure 1 shows the calculated photoabsorption cross section in Eq. (18) for ^{156}Gd and the contributions from different values of K. The transition strength depends on the value of K due to the deformation of ^{156}Gd. The excitation at low energy that can affect the neutron capture cross section mainly comes from the $K = \pm1$ mode. Without the contribution from Eq. (A3), the result is similar to the case without the residual interaction as in the case of double magic nuclei [25]. Such spin terms move the spin-flip strength to higher energies and separate contributions from the orbital and spin parts of Eq. (19). The strong peaks at 7.5 MeV and 9.8 MeV in Fig. 1 would reflect the double-humped structure as often found in heavy deformed nuclei [53].

The transition strength is usually used to compare calculations with experimental data. In our QRPA calculation, the $M1$ transition strength is given by

$$\frac{\mathrm{d}B(M1)}{\mathrm{d}E} = \sum_{K=0,\pm1} \frac{\mathrm{d}B(\omega; M_K)}{\mathrm{d}\omega}. \tag{27}$$

Figure 2 shows the results of Eq. (27) with and without the spin g factor $g_s^{(i)}$ in Eq. (19). It is clearly seen that the large strength in the 5 to 10 MeV range for orbital+spin (solid line) originated from the spin-flip $M1$ transition due to the finite value of $g_s^{(i)}$. The residual interaction induces the fragmentation of the spin-flip transitions and upshifts them up to about 15 MeV. From the energy integration of Eq. (27), the total transition strength from $E = 5$ MeV to 15 MeV is $\sum B(M1) = 29.4\mu_N^2$, which is larger than the typical value ($\sim 11\mu_N^2$) for heavy deformed nuclei [53]. Such overestimation of the total $M1$ transition strength is also reported by other published (Q)RPA calculations, and quenching of the spin g factor was proposed to improve the agreement with experimental data [21]. By applying a typical value of the quenching factor, $g_{s,\mathrm{eff}}^{(i)}/g_s^{(i)} = 0.6$–$0.7$ [54], the calculated $\sum B(M1)$ is reduced by a factor of 0.36–0.49, since the contribution from the spin-flip transition is proportional to the square of $g_s^{(i)}$ in Eq. (19).

As shown in the dotted line of Fig. 2, the contribution from orbital motion is not negligible at low energies. The transition strength near 3.3 MeV can be seen as the $M1$ scissors mode in a macroscopic view of the collective motion. For rare-earth nuclei, the scissors mode appears around 3 MeV, and the total transition strength is reported to be $\sum B(M1) \sim 3\mu_N^2$ [53]. In our QRPA calculation, we obtain $\sum B(M1) = 4.9\mu_N^2$ by integrating Eq. (27) up to 4 MeV. The difference between the solid and dotted lines in Fig. 2 implies that the contribution of spin part in Eq. (19) persists even at low energies. This suggests the overestimation of our calculated $\sum B(M1)$ might be reconciled by introducing the quench of $g_s^{(i)}$.

B. Spurious mode from $M1$ isoscalar operator

We discuss the role of elimination of the spurious mode following Sec. II C. In order to clarify the origin of the spurious mode, we separate the magnetic moments of nucleons in Eq. (19) by two parts such as the isoscalar (IS) and isovector (IV) operators [55],

$$\vec{\mu} = \mu_N \sum_{i=1}^{A} \left(g_s^{(i)} \frac{\vec{\sigma}_i}{2} + g_l^{(i)} \vec{l}_i \right) = \mu_N (\vec{\mu}_{\mathrm{IS}} + \vec{\mu}_{\mathrm{IV}}), \tag{28}$$

$$\vec{\mu}_{\mathrm{IS}} = \frac{1}{2}\vec{J} + \frac{g_s^p + g_s^n - 1}{2} \sum_{i=1}^{A} \frac{\vec{\sigma}_i}{2}, \tag{29}$$

$$\vec{\mu}_{\mathrm{IV}} = -\sum_{i=1}^{A} \tau_{zi} \vec{l}_i - \left(g_s^p - g_s^n \right) \sum_{i=1}^{A} \tau_{zi} \frac{\vec{\sigma}_i}{2}, \tag{30}$$

where $\vec{J} = \sum_{i=1}^{A} (\vec{l}_i + \vec{\sigma}_i/2)$ is the total angular momentum operator and τ_{zi} is $1/2(-1/2)$ for neutrons (protons).

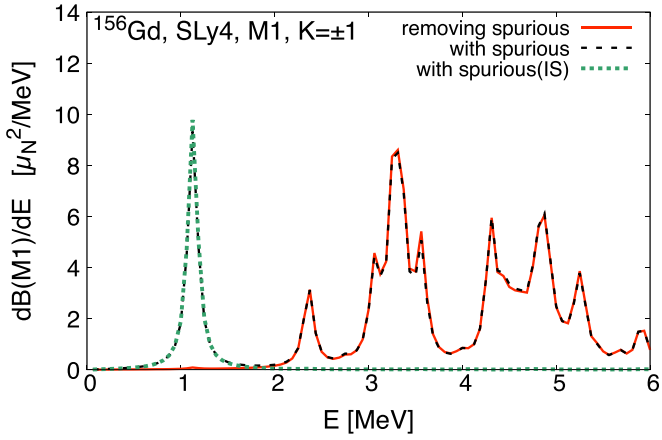

FIG. 3. The elimination of the spurious mode from the $M1$ scissors mode with Eq. (20). The solid line (dashed line) shows the result of $\sum_{K=\pm1} dB(\omega, M_K)/d\omega$ in the case with (without) removing the spurious mode. The dotted line shows the contribution from the isoscalar operator in Eq. (29) to the dashed line.

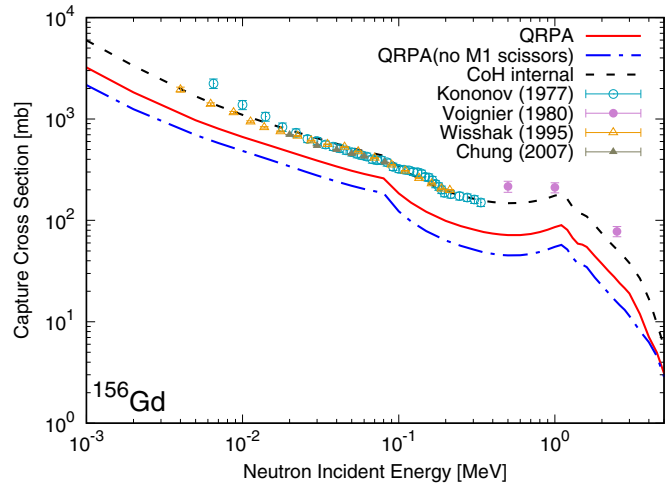

FIG. 4. The neutron capture cross sections on ^{156}Gd. The solid line shows the result of Eq. (24) with photoabsorption cross sections of the $E1$ and $M1$ transitions in QRPA. The dash-dotted line shows the result with QRPA cross sections neglecting the contribution from the $M1$ scissors mode ($E_\gamma \leqslant 4$ MeV) in Eq. (26) with $XL = M1$. The dashed line shows the result with CoH_3 internal strength functions. The symbols are available experimental data [60–63].

The solid line (dashed line) in Fig. 3 shows the result of $\sum_{K=\pm1} dB(\omega, M_K)/d\omega$ with (without) removing the spurious mode. By comparing these two lines, we can see the spurious mode at 1.2 MeV in the dashed line. Such $M1$ spurious mode at low energy is consistent with the result in Ref. [28]. The dotted line in Fig. 3 shows the result of $\sum_{K=\pm1} dB(\omega, M_K)/d\omega$ using only Eq. (29) without the elimination of the spurious mode. The dotted line is almost equivalent to the dashed line in $E < 2$ MeV and negligible at higher energy. Therefore, the IS mode gives rise to the spurious mode and hardly affects physical excitations. The spurious mode of the $M1$ transition is associated with the collective rotation of the whole nucleus around an axis perpendicular to the symmetry axis of the axially deformed nucleus [28] and $\vec{J}$ in Eq. (29) dominantly induces such a collective rotation. The contribution from the spin term in the IS mode is negligible due to the opposite signs of g_s^p and g_s^n. Such results of QRPA follow up a qualitative nature of the $M1$ transition as discussed in Ref. [18].

For the $M1$ transition, M_0 in Eq. (23) corresponds to the moment of inertia of the rotating nucleus [56]. We obtain $M_0 = 55$ MeV^{-1} for the calculation of ^{156}Gd with $F = M_{+1} - M_{-1}$ and underestimate the experimental moments inertia $\frac{2}{\hbar^2}\theta_{\rm exp} = 67.4$ MeV^{-1} [57]. Here, we use the surface pairing interaction dependent on the nucleon density for the HF+BCS calculation and the discrepancy could be improved with a different pairing model. For comparison with previous research, we calculate moments of inertia for erbium isotopes and our results are 10–20 % smaller than the volume pairing results in Ref. [56]. The calculated moments of inertia may increase if we relax the BCS approximation and consider the pairing fluctuation $\delta\Delta^{\pm}$.

C. Neutron capture reactions

We calculate the neutron capture cross sections for Gd isotopes following the discussion in Sec. II D. We use the coupled-channels Hauser-Feshbach code CoH_3 [58] with the γ-ray strength functions of various XL. As a default setting, CoH_3 employs the standard Lorentzian profiles for the $M1$, $E2$, $M2$, and $E3$ transitions and the generalized Lorentzian form [11] for the $E1$ transition. The large contribution to the γ-ray strength function comes from the $E1$ and $M1$ transitions, and the contributions from $E2$, $M2$, and $M3$ transitions are small in general. Here, we calculate both the $E1$ and $M1$ transitions for Gd isotopes with the same numerical setup as in Sec. III A and then apply the QRPA results to Eq. (26) to calculate the capture cross section instead of the CoH_3 internal strength functions. Note that the γ-ray strength functions of an even-odd nucleus, $(Z, A+1)$ are approximated to those of an even-even nucleus, (Z, A) when we calculate Eq. (24) of (Z, A) because the γ-ray strength function varies weakly as the target mass number [59]. It is commonly known that this approximation phenomenologically works well. However, it should be kept in mind that advanced theoretical frameworks for odd mass nuclei are favorable to calculate the fully microscopic γ-ray strength function of $(Z, A+1)$.

Figure 4 shows the calculated neutron capture cross sections on ^{156}Gd compared with experimental data. By comparing the solid and dash-dotted lines, we can see an enhancement of the calculated capture cross section caused by the $M1$ scissors mode in the low energy region ($E_\gamma \leqslant 4$ MeV) as in Ref. [15]. The calculated capture cross section is sensitive to the strengths of the excitations at a few MeV of E_γ because the level density of the compound state ρ in Eq. (25) increases with the excitation energy, $E_x = E_0 - E_\gamma$. The shapes of the two lines are similar in a wide range of neutron incident energy, and the difference in magnitude is characterized by the average γ-ray width $\langle\Gamma_\gamma\rangle$ calculated with the transmission coefficient in Eq. (25) and the average s-wave neutron level spacing D_0 [15]. The value of the $\langle\Gamma_\gamma\rangle$ for the

solid line (dash-dotted line) in Fig. 4 is 0.031 eV (0.019 eV), which indicates that the contribution from the scissors mode to the calculated capture cross section is $1 - 0.019/0.031 \approx 39\%$. Such a significant impact of the low energy $M1$ transition was also found in Refs. [15,16] and produces results in better agreement with the experimental data.

The calculated neutron capture cross section with the QRPA photoabsorption cross section is systematically lower than the experimental data, as shown in Fig. 4 by the solid line. For a quantitative discussion, the dashed line is the calculated capture cross section with the CoH_3 internal strength functions, which are globally parameterized giant resonances adjusted to available experimental data. The average γ-ray width of CoH_3 internal is $\langle\Gamma_\gamma\rangle = 0.067$ eV so our QRPA result underestimates the capture cross section by $\frac{0.031}{0.067} \approx 46\%$.

Although we demonstrated this for ^{156}Gd, almost the same properties are confirmed for other stable Gd isotopes. For example, Figs. 5(a) and 5(b) show neutron capture cross sections on ^{157}Gd and ^{158}Gd. The values of $\langle\Gamma_\gamma\rangle$ for QRPA (solid line), QRPA without the scissors mode (dash-dotted line), and CoH_3 internal (dashed line) are summarized in Table I. The shapes of these three calculated results are similar over a wide range of neutron incident energy, but the magnitudes are different. For ^{157}Gd(^{158}Gd), the scissors mode contributes to about 38(42)% of the QRPA capture cross section. Since these Gd isotopes are well deformed, the effect of the $M1$ scissors is prominent. However, the contribution of the low energy $M1$ transition becomes small on a spherical nucleus (e.g., ^{144}Sm) because the $M1$ scissors mode is negligible and only the spin-flip transition contributes to $f_{M1}(E_\gamma)$. The QRPA result is about 37(42)% of the experimental data for ^{157}Gd(^{158}Gd). Although we limit ourselves to deformed Gd isotopes in this paper, further systematic studies for both spherical and deformed nuclei enable a more quantitative discussion on such an underestimation of stable nuclei.

Figure 5(c) shows the calculated capture cross sections on an unstable nucleus ^{161}Gd nearby a stable region. For the QRPA calculations (solid line and dash-dotted line), we use the QRPA photoabsorption cross sections on ^{162}Gd. The $M1$ scissors mode has a large contribution (∼50%) on the QRPA result due to the large nuclear shape deformation. The QRPA result (solid line) is about 35% of CoH_3 (dashed line) and the value with microscopic model is smaller than that of the phenomenological model as found on the stable Gd isotopes. To discuss the importance of the microscopic model on various unstable nuclei, we first need an improvement to resolve discrepancies with experimental data on stable Gd isotopes.

TABLE I. The values of $\langle\Gamma_\gamma\rangle$ (in eV) for QRPA, QRPA without the scissors mode, and CoH_3 internal on Gd isotopes.

Nucleus	QRPA	QRPA(no $M1$ scissors)	CoH_3
^{156}Gd	0.031	0.019	0.067
^{157}Gd	0.029	0.018	0.078
^{158}Gd	0.031	0.018	0.073
^{161}Gd	0.014	0.007	0.040

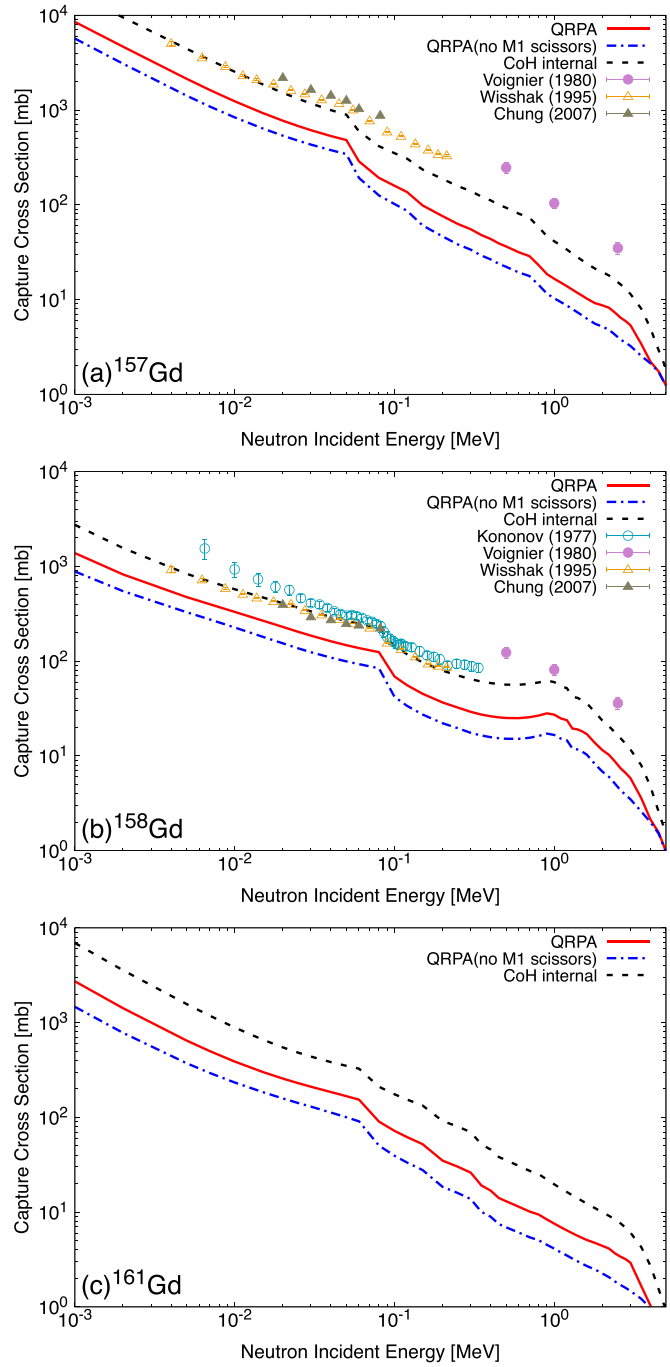

FIG. 5. Same as in Fig. 4, but for ^{157,158,161}Gd.

Furthermore, our approximation of the γ-ray strength function of an even-odd nucleus, $(Z, A+1)$ is not necessarily valid for very neutron-rich unstable nuclei, and the QRPA calculation applicable to odd mass nuclei is favorable for more reliable prediction.

Figure 6 shows the employed $E1$ and $M1$ cross sections for both QRPA (solid line) and CoH_3 internal (dashed line) in Fig. 4. The QRPA result of the $E1$ transition (solid line) in Fig. 6 reproduces well the split of GDR peaks for deformed nuclei as in Ref. [25]. The tail on the lower side of GDR

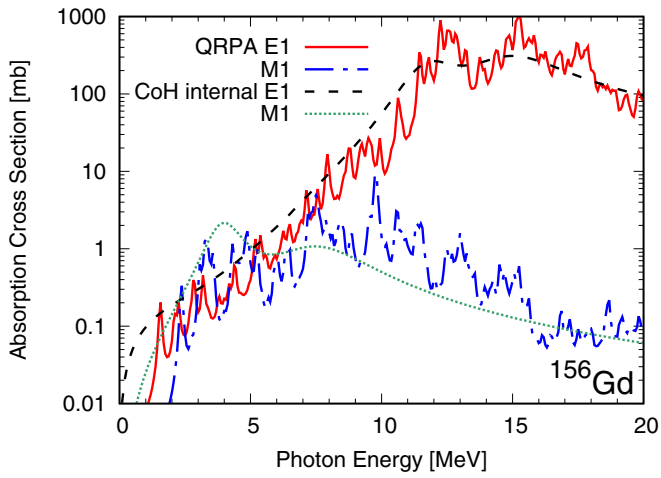

FIG. 6. The photoabsorption cross sections of $E1$ and $M1$ transitions for ^{156}Gd, which are employed to calculate the neutron capture cross sections shown by the solid and dashed lines in Fig. 4.

dominantly contributes to Eq. (25) due to the large $\rho(E_x, j^\pi)$, and the solid line is smaller than the dashed line at small photon energy, which results in the underestimation of the QRPA result in Fig. 4. Here, we emphasize that the underestimation problem can hardly be resolved by the theoretical improvement of the microscopic $M1$ calculation alone, because, as discussed in Sec. III A, our QRPA calculation overestimates the value of $\sum B(M1)$ for the scissors mode so a more realistic calculation is supposed to reduce the values of both the $\sum B(M1)$ and $\langle\Gamma_\gamma\rangle$, which is against the situation of neutron capture cases. We may envisage uncertainties in the $E1$ transition at low energies also impact the calculated capture cross sections. The $E1$ transition strength in QRPA should be enhanced by 3–5 times to reproduce the calculated capture cross section of CoH_3 internal. We used a fixed Lorentzian width, $\gamma = 125$ keV for our QRPA calculation, but the energy and temperature-dependent width [11] may affect the low energy tail of the GDR. The toroidal dipole resonance is predicted in the same energy region of the pygmy resonance [64], and such a low energy $E1$ excitation can be involved in our QRPA by considering the second-order terms of the $E1$ operator ignored in the long-wavelength limit [65]. Furthermore, the calculated capture cross section can be enhanced in the microscopic calculations considering the phonon coupling as in quasiparticle time blocking approximation (QTBA) [66] and quasiparticle-phonon model (QPM) [67]. The implicit violation of the generalized Brink-Axel hypothesis was suggested (e.g., Refs. [68,69]), and a partial breakdown of the hypothesis could be another possible improvement of Eq. (26).

It is also plausible that the assumption of $E = E_\gamma$ for $\omega = E + i\gamma/2$ in Eqs. (26) and (27) might need some corrections due to the rotational energy $\Delta E_{\rm rot}$ such as $E = E_\gamma + \Delta E_{\rm rot}$. The γ-ray strength function becomes large even near $E_\gamma = 0$ when $\Delta E_{\rm rot} > 0$, which might improve the underestimation problem. Note that our technique to eliminate the $M1$ spurious mode associated with the collective rotation partly accounts for such a rotational correction.

IV. CONCLUSION

We extended our noniterative FAM-RPA to the framework of FAM-QRPA with the HF+BCS single-particle states and solved the QRPA equation to study the $M1$ transition for deformed gadolinium isotopes. We showed large spin-flip transitions from 5 to 10 MeV and the orbital transition around 3 MeV where the $M1$ scissors mode was experimentally confirmed in the deformed rare-earth nuclei. We demonstrated that the spurious mode of the $M1$ transition originated from the IS part of the $M1$ operator. Although our result overestimates the total $M1$ transition strength, it can be reduced when we consider quenching of the spin g factor as proposed in previous QRPA studies.

Finally we applied the QRPA results of $E1$ and $M1$ transitions to calculations of neutron capture reactions based on the statistical Hauser-Feshbach theory. The low energy $M1$ transition contributes to about half of the total calculated capture cross section, and our calculation underestimates the capture cross section by 30–50 % compared with the experimental data. Improvements in the cross section would probably be possible by considering some uncertainty of the low energy $E1$ transition neglected in our QRPA calculation. This we leave for future work.

ACKNOWLEDGMENTS

This work was partially support by the Office of Defense Nuclear Nonproliferation Research & Development (DNN R&D), National Nuclear Security Administration, U.S. Department of Energy. This work was carried out under the auspices of the National Nuclear Security Administration of the U.S. Department of Energy at Los Alamos National Laboratory under Contract No. 89233218CNA000001.

APPENDIX: SPIN TERMS IN THE RESIDUAL INTERACTION

In QRPA calculation, we consider the contribution from spin terms in the Skyrme forces ignored in our previous RPA calculation [25]. The Skyrme energy density, $\mathcal{H}_{\rm Sk}$ includes the spin terms labeled with $\tilde{b}_i, \tilde{b}'_i (i = 0, 2, 3)$ [26],

$$\begin{aligned}\mathcal{E}_{\rm spin} = &\frac{\tilde{b}_0}{2}|\vec{s}|^2 - \frac{\tilde{b}'_0}{2}\sum_q |\vec{s}_q|^2 \\ &+ \frac{\tilde{b}_3}{3}\rho^\alpha|\vec{s}|^2 - \frac{\tilde{b}'_3}{3}\rho^\alpha\sum_q|\vec{s}_q|^2 \\ &- \frac{\tilde{b}_2}{2}\vec{s}\cdot\Delta\vec{s} + \frac{\tilde{b}'_2}{2}\sum_q \vec{s}_q\cdot\Delta\vec{s}_q, \end{aligned} \tag{A1}$$

where $\vec{s} = \vec{s}_n + \vec{s}_p$ is the summation of the spin density of nucleon $q(= n, p)$,

$$\vec{s}_q = \eta\sum_{\substack{\alpha\beta\in q\\ \alpha\geqslant\beta}} \zeta^-_{\alpha\beta}\left(\phi^{q*}_\beta\vec{\sigma}\phi^q_\alpha X^q_{\alpha\beta} + \phi^{q*}_\alpha\vec{\sigma}\phi^q_\beta Y^q_{\alpha\beta}\right) + O(\eta^2), \tag{A2}$$

where $\phi^{q*}_{\bar{\alpha}}\vec{\sigma}\phi^q_{\bar{\beta}} = -\phi^{q*}_\beta\vec{\sigma}\phi^q_\alpha$ is used in the summation of α, β. The b coefficients in Eq. (A1) can be described in

terms of t and x coefficients in the Skyrme forces [70]. The functional derivatives such as $\delta/\delta\vec{s}_q(\int \mathrm{d}^3 r\mathcal{E}_{\mathrm{spin}})$ and $\delta/\delta\rho_q(\int \mathrm{d}^3 r\mathcal{E}_{\mathrm{spin}})$ generally induce potentials in the single-particle Hamiltonian for static calculations [70]. In the case of even-even nuclei satisfying the time-reversal symmetry, the time-odd potentials derived from such functional derivatives do not affect the static HF+BCS calculation. However, in dynamical calculations like (Q)RPA, the second derivative $\delta^2/\delta\vec{s}_q\delta\vec{s}_{q'}(\int \mathrm{d}^3 r\mathcal{E}_{\mathrm{spin}})$ can induce a residual interaction in δh^{odd} [26]. The contribution from Eq. (A1) to an integral term proportional to $\zeta^-_{\mu\nu}\zeta^-_{\alpha\beta}$ in Eq. (11) is written as

$$
\begin{aligned}
&(\tilde{b}_0 - \delta_{qq'}\tilde{b}'_0)\int \mathrm{d}^3 r\left(\phi^{q*}_\mu \vec{\sigma}\phi^q_\nu\right)\cdot\left(\phi^{q'*}_\beta \vec{\sigma}\phi^{q'}_\alpha\right) + (\tilde{b}_3 - \delta_{qq'}\tilde{b}'_3)\int \mathrm{d}^3 r\,\frac{2}{3}(\rho_0)^\alpha\left(\phi^{q*}_\mu \vec{\sigma}\phi^q_\nu\right)\cdot\left(\phi^{q'*}_\beta \vec{\sigma}\phi^{q'}_\alpha\right)\\
&+(\tilde{b}_2 - \delta_{qq'}\tilde{b}'_2)\int \mathrm{d}^3 r\,\nabla\left(\phi^{q*}_\mu \vec{\sigma}\phi^q_\nu\right)\cdot\nabla\left(\phi^{q'*}_\beta \vec{\sigma}\phi^{q'}_\alpha\right),
\end{aligned}
\tag{A3}
$$

where $\rho_0 = (\rho_n + \rho_p)_{\eta=0}$ in Eq. (16). The effect on Eq. (12) is easily derived from an exchange, $(\phi^{q'*}_\beta \vec{\sigma}\phi^{q'}_\alpha) \to (\phi^{q'*}_\beta \vec{\sigma}\phi^{q'}_\alpha)^*$ in Eq. (A3). In our QRPA calculation, ϕ^q_μ is expanded in the cylindrical coordinate space as in Ref. [44] and the above residual interaction is calculated in analogy with our previous RPA calculation [25].

[1] M. E. Burbidge, G. R. Burbidge, W. A. Fowler, and F. Hoyle, Rev. Mod. Phys. **29**, 547 (1957).
[2] M. R. Mumpower, R. Surman, G. C. McLaughlin, and A. Aprahamian, Prog. Part. Nucl. Phys. **86**, 86 (2016).
[3] C. Kobayashi, A. I. Karakas, and M. Lugaro, Astrophys. J. **900**, 179 (2020).
[4] C. Fröhlich, G. Martínez-Pinedo, M. Liebendörfer, F.-K. Thielemann, E. Bravo, W. R. Hix, K. Langanke, and N. T. Zinner, Phys. Rev. Lett. **96**, 142502 (2006).
[5] H. Sasaki, T. Kajino, T. Takiwaki, T. Hayakawa, A. B. Balantekin, and Y. Pehlivan, Phys. Rev. D **96**, 043013 (2017).
[6] H. Sasaki, Y. Yamazaki, T. Kajino, M. Kusakabe, T. Hayakawa, M.-K. Cheoun, H. Ko, and G. J. Mathews, Astrophys. J. **924**, 29 (2022).
[7] S. E. Woosley, D. H. Hartmann, R. D. Hoffman, and W. C. Haxton, Astrophys. J. **356**, 272 (1990).
[8] T. Hayakawa, H. Ko, M.-K. Cheoun, M. Kusakabe, T. Kajino, M. D. Usang, S. Chiba, K. Nakamura, A. Tolstov, K. Nomoto, M.-a. Hashimoto, M. Ono, T. Kawano, and G. J. Mathews, Phys. Rev. Lett. **121**, 102701 (2018).
[9] H. Ko, D. Jang, M.-K. Cheoun, M. Kusakabe, H. Sasaki, X. Yao, T. Kajino, T. Hayakawa, M. Ono, T. Kawano, and G. J. Mathews, Astrophys. J. **937**, 116 (2022).
[10] W. Hauser and H. Feshbach, Phys. Rev. **87**, 366 (1952).
[11] J. Kopecky and M. Uhl, Phys. Rev. C **41**, 1941 (1990).
[12] D. M. Brink, D. Phil. thesis, Oxford University, 1955.
[13] J. Kopecky, M. Uhl, and R. E. Chrien, Phys. Rev. C **47**, 312 (1993).
[14] J. L. Ullmann, T. Kawano, T. A. Bredeweg, A. Couture, R. C. Haight, M. Jandel, J. M. O'Donnell, R. S. Rundberg, D. J. Vieira, J. B. Wilhelmy, J. A. Becker, A. Chyzh, C. Y. Wu, B. Baramsai, G. E. Mitchell, and M. Krtička, Phys. Rev. C **89**, 034603 (2014).
[15] M. R. Mumpower, T. Kawano, J. L. Ullmann, M. Krtička, and T. M. Sprouse, Phys. Rev. C **96**, 024612 (2017).
[16] S. Goriely, S. Hilaire, S. Péru, and K. Sieja, Phys. Rev. C **98**, 014327 (2018).
[17] D. Bohle, A. Richter, W. Steffen, A. E. L. Dieperink, N. Lo Iudice, F. Palumbo, and O. Scholten, Phys. Lett. B **137**, 27 (1984).
[18] K. Heyde, P. von Neumann-Cosel, and A. Richter, Rev. Mod. Phys. **82**, 2365 (2010).
[19] P. Ring and P. Schuck, *The Nuclear Many-Body Problem*, Physics and Astronomy Online Library (Springer, New York, 2004).
[20] D. Rowe, *Nuclear Collective Motion: Models and Theory* (World Scientific, Singapore, 2010).
[21] M. Harakeh and A. Woude, *Giant Resonances: Fundamental High-frequency Modes of Nuclear Excitation* (Oxford University Press, Oxford, 2001).
[22] K. Yoshida and T. Nakatsukasa, Phys. Rev. C **83**, 021304(R) (2011).
[23] T. Inakura, T. Nakatsukasa, and K. Yabana, Phys. Rev. C **80**, 044301 (2009).
[24] T. Oishi, M. Kortelainen, and N. Hinohara, Phys. Rev. C **93**, 034329 (2016).
[25] H. Sasaki, T. Kawano, and I. Stetcu, Phys. Rev. C **105**, 044311 (2022).
[26] P. Vesely, J. Kvasil, V. O. Nesterenko, W. Kleinig, P. G. Reinhard, and V. Y. Ponomarev, Phys. Rev. C **80**, 031302(R) (2009).
[27] V. O. Nesterenko, J. Kvasil, P. Vesely, W. Kleinig, P. G. Reinhard, and V. Y. Ponomarev, J. Phys. G **37**, 064034 (2010).
[28] A. Repko, J. Kvasil, and V. O. Nesterenko, Phys. Rev. C **99**, 044307 (2019).
[29] V. Tselyaev, N. Lyutorovich, J. Speth, P. G. Reinhard, and D. Smirnov, Phys. Rev. C **99**, 064329 (2019).
[30] V. O. Nesterenko, P. I. Vishnevskiy, J. Kvasil, A. Repko, and W. Kleinig, Phys. Rev. C **103**, 064313 (2021).
[31] V. O. Nesterenko, P. I. Vishnevskiy, A. Repko, and J. Kvasil, Phys. At. Nucl. **85**, 858 (2022).
[32] T. Nakatsukasa, T. Inakura, and K. Yabana, Phys. Rev. C **76**, 024318 (2007).
[33] P. Avogadro and T. Nakatsukasa, Phys. Rev. C **84**, 014314 (2011).
[34] M. Stoitsov, M. Kortelainen, T. Nakatsukasa, C. Losa, and W. Nazarewicz, Phys. Rev. C **84**, 041305(R) (2011).
[35] N. Hinohara, M. Kortelainen, and W. Nazarewicz, Phys. Rev. C **87**, 064309 (2013).
[36] M. Kortelainen, N. Hinohara, and W. Nazarewicz, Phys. Rev. C **92**, 051302(R) (2015).

[37] H. Liang, T. Nakatsukasa, Z. Niu, and J. Meng, Phys. Rev. C **87**, 054310 (2013).
[38] T. Nikšić, N. Kralj, T. Tutiš, D. Vretenar, and P. Ring, Phys. Rev. C **88**, 044327 (2013).
[39] M. T. Mustonen, T. Shafer, Z. Zenginerler, and J. Engel, Phys. Rev. C **90**, 024308 (2014).
[40] T. Shafer, J. Engel, C. Fröhlich, G. C. McLaughlin, M. Mumpower, and R. Surman, Phys. Rev. C **94**, 055802 (2016).
[41] E. M. Ney, J. Engel, T. Li, and N. Schunck, Phys. Rev. C **102**, 034326 (2020).
[42] N. Hinohara and J. Engel, Phys. Rev. C **105**, 044314 (2022).
[43] K. Washiyama, N. Hinohara, and T. Nakatsukasa, Phys. Rev. C **103**, 014306 (2021).
[44] D. Vautherin, Phys. Rev. C **7**, 296 (1973).
[45] W. Greiner and J. A. Maruhn, *Nuclear Models* (Springer, Berlin, 1996).
[46] J. A. Maruhn, P. G. Reinhard, P. D. Stevenson, and A. S. Umar, Comput. Phys. Commun. **185**, 2195 (2014).
[47] P. Avogadro and T. Nakatsukasa, Phys. Rev. C **87**, 014331 (2013).
[48] I. Stetcu and C. W. Johnson, Phys. Rev. C **67**, 044315 (2003).
[49] T. Kawano, P. Talou, and H. A. Weidenmüller, Phys. Rev. C **92**, 044617 (2015).
[50] L. Bonneau, T. Kawano, T. Watanabe, and S. Chiba, Phys. Rev. C **75**, 054618 (2007).
[51] T. Duguet, P. Bonche, and P. H. Heenen, Nucl. Phys. A **679**, 427 (2001).
[52] E. Chabanat, P. Bonche, P. Haensel, J. Meyer, and R. Schaeffer, Nucl. Phys. A **635**, 231 (1998).
[53] A. Richter, Prog. Part. Nucl. Phys. **34**, 261 (1995).
[54] G. Kružić, T. Oishi, D. Vale, and N. Paar, Phys. Rev. C **102**, 044315 (2020).
[55] A. Richter, Nucl. Phys. A **507**, 99 (1990).
[56] K. Petrík and M. Kortelainen, Phys. Rev. C **97**, 034321 (2018).
[57] L. Lin, Phys. Rev. C **51**, 3017 (1995).
[58] T. Kawano, Eur. Phys. J. A **57**, 16 (2021).
[59] S. Goriely *et al.*, Eur. Phys. J. A **55**, 172 (2019).
[60] V. N. Kononov, B. D. Yurlov, G. N. Manturov, E. Poletaev, V. M. Timokhov, and V. S. Shorin, Yadernye Konstanty **22**, 29 (1977).
[61] J. Voignier, S. Joly, G. Grenier, D. M. Drake, and L. Nilsson, Centre d'Etudes Nucleaires, Saclay Reports (1981), p. 5089.
[62] K. Wisshak, F. Voss, F. Käppeler, K. Guber, L. Kazakov, N. Kornilov, M. Uhl, and G. Reffo, Phys. Rev. C **52**, 2762 (1995).
[63] J. Nishiyama, T.-I. Ro, M. Igashira, W.-C. Chung, G. Kim, T. Ohsaki, S. Lee, and T. Katabuchi, *International Conference on Nuclear Data for Science and Technology* (2007), pp. 615–618.
[64] A. Repko, V. O. Nesterenko, J. Kvasil, and P. G. Reinhard, Eur. Phys. J. A **55**, 242 (2019).
[65] J. Kvasil, V. O. Nesterenko, W. Kleinig, P. G. Reinhard, and P. Vesely, Phys. Rev. C **84**, 034303 (2011).
[66] A. Avdeenkov, S. Goriely, S. Kamerdzhiev, and S. Krewald, Phys. Rev. C **83**, 064316 (2011).
[67] N. Tsoneva, S. Goriely, H. Lenske, and R. Schwengner, Phys. Rev. C **91**, 044318 (2015).
[68] C. W. Johnson, Phys. Lett. B **750**, 72 (2015).
[69] R. A. Herrera, C. W. Johnson, and G. M. Fuller, Phys. Rev. C **105**, 015801 (2022).
[70] M. Bender, P.-H. Heenen, and P.-G. Reinhard, Rev. Mod. Phys. **75**, 121 (2003).